Engineered Science

RESEARCH PAPER View Article Online

Investigation on the Distribution of Fe and Ni in Reduced Mo Powders and Its Effects on the Activated Sintering of Mo Compacts

Haidong Hu, Qiao Yin, Shuqun Chen,* Yanlin Jia, Wenyuan Zhou, Hongyi Li, Peng Hu and Jinshu Wang*

In this article, high densification Mo-1.0 wt.% Fe and Mo-1.0 wt.% Ni alloys were fabricated by a powder metallurgy technique. The distribution, chemical states and evolution of the doping elements within molybdenum powders were systematically investigated by serial analytical techniques, before further correlating to the microstructural development of solid-state sintered molybdenum compacts. The results indicated that after liquid-solid doping processing both Fe and Ni had been incorporated into the lattice sites of MoO_3 and formed metal molybdates onto the surfaces of MoO_3. The following hydrogen reduction produced nanometer thick Mo(Fe) solid solutions and $Mo_{0.25}Ni_{0.75}$ films at surfaces of Mo powders. Solid-state activated sintering was occurred in Fe/Ni doped Mo compacts under a sintering temperature of 1400 ºC. It was found that Fe remained at grain boundaries as Mo(Fe) solid solution in Mo-Fe alloy, which enabled to promote the diffusion of Mo atoms because of a lower vacancy formation energy. Grain boundary segregation of NiMo compound was identified in Mo-Ni alloy. This NiMo layer was transformed from the $Mo_{0.25}Ni_{0.75}$ coating in reduced Mo powders and served as a short-circuit diffusion paths for Mo atoms throughout sintering.

Keywords: Powder metallurgy; Molybdenum alloy; Transition metal; Activated sintering

Received 19 December 2018**, Accepted** 8 January 2019

DOI: 10.30919/es8d686

1. Introduction

Molybdenum (Mo) and its alloys have been extensively utilized for ultra-high temperature components such as furnace parts, isothermal forging dies and electrodes for melting glass due to their unique physical properties including high melting point, low thermal-expansion coefficient, good thermal conductivity and high mechanical strength at elevated temperatures.[1–3] Like most of the refractory metals, molybdenum is mainly produced by powder metallurgical (PM) procedures,[2] in which field or chemical activated sintering have been often employed to facilitate the densification process. For example, spark plasma sintering (SPS) could take a few minutes to complete the sintering cycle of Mo, which is much faster compared to conventional sintering route. [4,5] But the requirement of costly SPS instruments and the limitation of specimen shape restrict its industrial applications.[6] Chemical activated sintering on the other hand is easier for molybdenum compacts to consolidate. The small addition of transition metal elements (*i.e.* Fe and Ni) has been reported to effectively lower the sintering temperature and enhance the sintered density of Mo.[7,8]

Active elements can be added into refractory metal powders by a variety of approaches, such as blending in V-shaped mixer,[9] mechanical alloying,[10] sol-spray drying,[11] and liquid-solid method. [12] Depending on the fabrication method selected, the distribution and chemical states (*i.e.* solid solution or intermetallic compound, particles or coatings) of the activators within Mo powders are highly likely to be different, whereby the identification of these elemental information becomes essential since they could affect the following sintering behaviours in a distinct way. Taking the preparation of tungsten heavy alloy as an example, it is ideal to coat the nickel onto tungsten powders to avoid compositional segregation, as often observed in the blended composite powders, and thus improve the overall performance.[13] However, to our best knowledge, few studies have been attempted to clarify this for transition metal-doped molybdenum.

In this paper, 1.0 wt.% Fe or 1.0 wt.% Ni doped Mo alloys were prepared by a liquid-solid method and a subsequent powder metallurgy processing. The distribution and chemical states of alloying elements within concerned powders and compacts were systematically investigated by serial analytical techniques, before further correlating to the microstructural development of solid-state sintered molybdenum compacts. This research aims at contributing more knowledge on the chemical activated sintering in refractory metal system.

2. Experimental

$Fe(NO_3)_3·9H_2O$ (99.99 wt.%, Aladdin Chemical Co. Ltd., China), $NiCl_2·6H_2O$ (99.9 wt.%, Aladdin Chemical Co. Ltd., China) and MoO_3 (1-3 μm, 99.99 wt.%, Ganzhou Kemingrui Non-Ferrous Metal Materials Co. Ltd., China) were used as starting materials. The molybdenum alloys with Fe/Ni were fabricated by a liquid-solid method

College of Materials Science and Engineering, Key Laboratory of Advanced Functional Materials, Education Ministry of China, Beijing University of Technology, Beijing 100124, China
***E-mail:** chensq@bjut.edu.cn; wangjsh@bjut.edu.cn*

Table 1 Nominal composition and structural parameters for the studied samples.

Sample I.D.	Doping content in Mo powders		Lattice parameters of MoO_3 powders			Density of Mo compacts
	Fe (wt.%)	Ni (wt.%)	a (Å)	b (Å)	c (Å)	(%)
M1	0	0	3.915	13.840	3.685	83.5
M2	1.0	0	3.916	13.844	3.685	90.9
M3	0	1.0	3.955	13.820	3.693	97.2

and a subsequent PM procedure. The composition and the abbreviation of the samples are shown in Table 1. Firstly, a mixture solution containing 4.86 g $Fe(NO_3)_3 \cdot 9H_2O$ or 2.71 g $NiCl_2 \cdot 6H_2O$ and 100 g MoO_3 in 500 mL deionized water was prepared by continuous stirring. Then the solution was placed into a water bath pan at 100 °C for solvent evaporation, whereby dried MoO_3 powders with alloying elements were readily collected. Having calcined at 600 °C for 2 h in air, the doped MoO_3 powders were reduced by hydrogen at 500 °C and 900 °C for 2 h, respectively, to synthesize doped Mo powders. Finally, the Mo-Fe and Mo-Ni composite powders were pressed into cylinder compacts and sintered at 1400 °C for 1 h under hydrogen atmosphere. Pure Mo was also prepared under identical procedures for comparison.

The sintered densities were measured according to Archimedes principle. The microstructures of prepared powders and compacts were characterized by X-ray diffraction (XRD, Bruker D8), scanning electron microscopy (SEM, Hitachi-S4800), high angle annular dark field scanning transmission electron microscopy (HAADF-STEM, FEI Tecnai G2 F30) and selected-area electron diffraction (SAED). The elemental information was analysed by X-ray photoelectron spectroscopy (XPS, Thermal Scientific ESCALAB 250XI), Energy-dispersive X-ray spectroscopy (EDS, Oxford Instrument) and auger electron spectroscopy (AES, ULVAC-PHI PHI-700).

3. Results and discussion

3.1 Incorporation of Fe and Ni into MoO_3 powders

Fig. 1a shows the XRD patterns of pure and doped molybdenum oxides after calcinations in air at 600 ºC. Compared with the data in JCPDS 35-0609, the profound peaks appeared at ~ 12.82°, 23.37°, 25.73°, 27.36° and 39.01° can be indexed to the planes of (020), (110), (040), (021) and (060) in α-MoO_3 with orthorhombic structures.[14] The strong intensities of (0 k 0) reflections with k = 2, 4, and 6 indicate the existence of the lamellar structure.[15] In addition to the matrix phase, weak diffraction peaks of $Fe_2(MoO_4)_3$ (JCPDS 35-0183) and $NiMoO_4$ (JCPDS 86-0361) were identified for M2 and M3, respectively. The lattice parameters of three concerned samples were calculated and are listed in Table 1. It shows that pure MoO_3 and Fe-doped MoO_3 display similar lattice constants, while a and b parameters are variation in Ni-doped specimen, indicating a lattice deformation caused by the

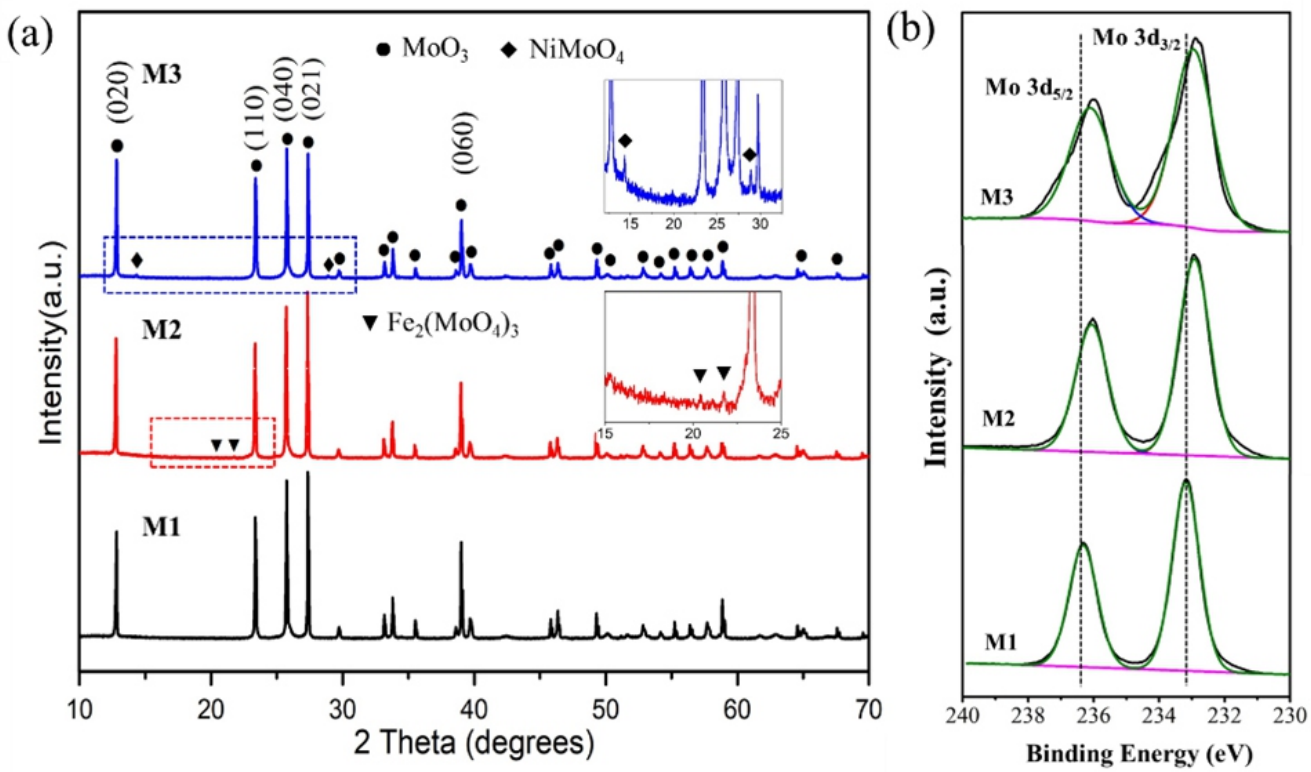

Fig. 1 XRD patterns (a) and XPS spectra (b) of as-prepared MoO_3 powders after calcinations at 600 °C. Insert images are the close views of peaks marked in the rectangles.

substitution of Ni ions for the Mo sites in the MoO_3 structure.[16,17] However, it is still unclear whether Fe has been doped into MoO_3 lattice since the ionic radius of Fe^{3+} (0.645 Å) is very close to that of Mo^{6+} (0.65 Å).[18]

To better demonstrate the chemical state of concerned elements, XPS analysis was carried out using C 1s peak at binding energy (BE) of 284.6 eV as a reference. As shown in Fig. 1b, the high-resolution Mo 3d spectrum in pure MoO_3 are characterized by two spin orbit components Mo $3d_{5/2}$ (BE = 233.2 eV) and $3d_{3/2}$ (BE = 236.3 eV). The binding energy peaks of Mo 3d are separated by 3.1 eV, which is a signature of Mo^{6+} oxidation state.[19] A progressive shift to lower binding energy of Mo 3d peaks is observed in the spectra of M2 and M3, indicating the existence of Mo^{5+} ions at surfaces.[20] The latter is due to the fact that doping with Fe or Ni within lattice have changed the stoichiometry of MoO_3, whereby oxygen vacancies and less charged Mo cations are prone to be formed to maintain the electrical neutrality.[21] In addition, the core region spectra of Fe 2p in M2 and Ni 2p in M3 (see Fig. S1) reveal that they consist of spin-orbit doublet peaks in agreement with Fe^{3+} and Ni^{2+} oxidation states, respectively.[22,23] Combining the XPS and XRD analysis restuls, we could infer that certain Fe and Ni atoms may have been incorporated into the lattice sites of MoO_3, while excess impurity atoms form secondary phases of $Fe_2(MoO_4)_3$ and $NiMoO_4$.

The morphologies of the synthesized MoO_3 products were investigated by a scanning electron microscope, as illustrated in Fig. 2a-c. It is evident that pure MoO_3 is composed of elongated lamellar plates. The maximum length and width of the plates could reach 25 μm and 10 μm, respectively. This morphology however is far from visible from the as-received MoO_3 (see Fig. S2), demonstrating an effective grain growth during the annealing treatment. After doping elements were introduced, the microstructures of MoO_3 become refined and more particles are irregular in shape. Fig. 2d-e depict the high-magnification SEM images for two doped samples, in which spherical particles (100-200 nm in size) with bright contrast are clearly observed. The corresponding EDS results confirm that these nanoparticles contain Fe and Ni, respectively, and thus can be assigned to the $Fe_2(MoO_4)_3$ and $NiMoO_4$ concerned. Considering that EDS spot diameter is about several microns,[24] more signals from the MoO_3 matrix would be collected although point-scanning was performed on these nanoparticles. This explains low atomic ratios of impurity atoms in Fig. 2d-e.

The formation procedures for $Fe_2(MoO_4)_3$ and $NiMoO_4$ can be potentially explained according to the Eqs. (1) to (6), which were happened during the water bath heating and thermal annealing treatments. It is noteworthy that α-MoO_3 with tertiary large layers (upto tens of micrometres) are formed from the stacking of secondary layers with an average thickness of several tens of nanometres, where the adjacent layers along [010] are linked particularly due to weak van der Waals forces to make the lamellar formation.[25,26] In this case, the existence of Fe or Ni based species may affect the stacking behaviours of MoO_3 during annealing, resulting into refined microstructures.

$$Fe(NO_3)_3 + 3H_2O \xrightarrow{100^{\circ}C} Fe(OH)_3 + 3HNO_3\uparrow \quad (1)$$

$$2Fe(OH)_3 \xrightarrow{600^{\circ}C} Fe_2O_3 + 3H_2O\uparrow \quad (2)$$

$$MoO_3 + Fe_2O_3 \xrightarrow{600^{\circ}C} Fe_2(MoO_4)_3 + Fe\text{-}MoO_{3-x} \quad (3)$$

$$NiCl_2 + 2H_2O \xrightarrow{100^{\circ}C} Ni(OH)_2 + 2HCl\uparrow \quad (4)$$

$$Ni(OH)_2 \xrightarrow{600^{\circ}C} NiO + H_2O\uparrow \quad (5)$$

$$MoO_3 + NiO \xrightarrow{600^{\circ}C} NiMoO_4 + Ni\text{-}MoO_{3-x} \quad (6)$$

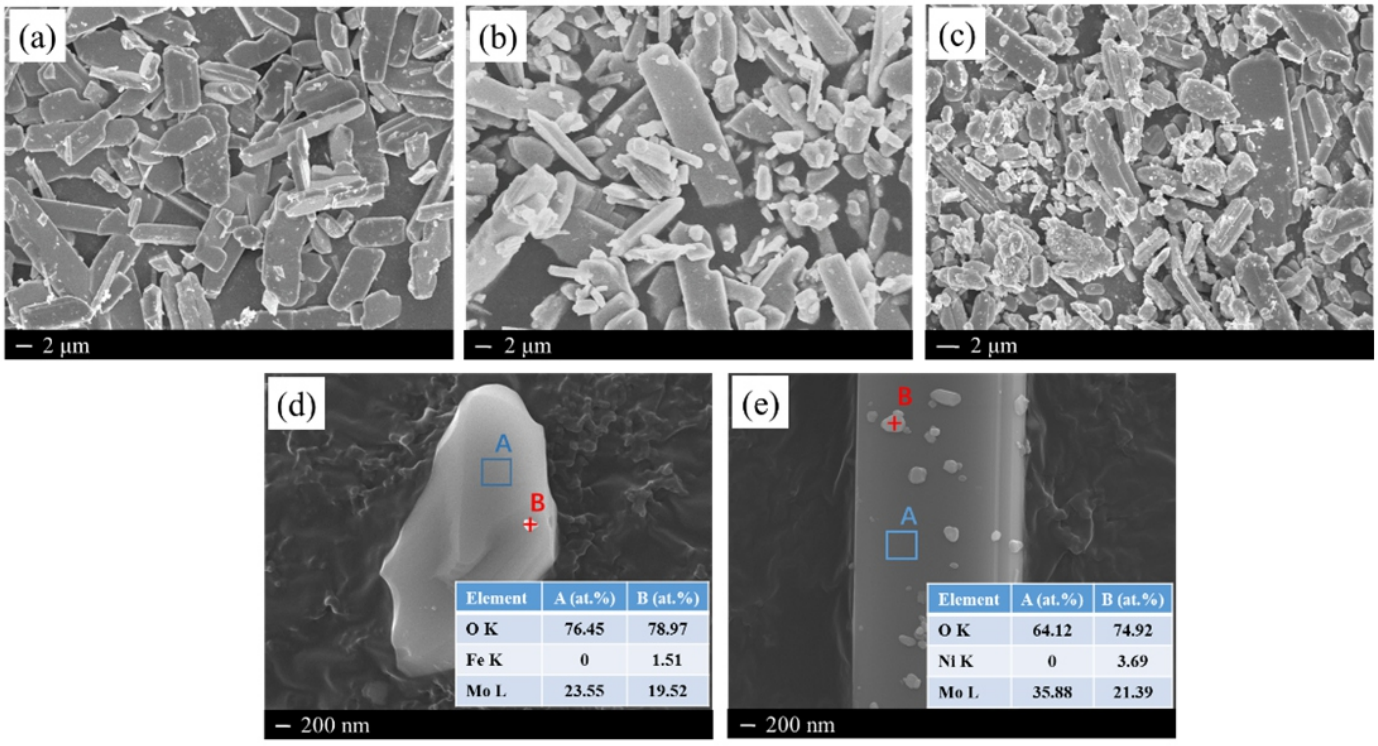

Fig. 2 SEM images and EDS results of as-prepared MoO_3 powders: (a) M1, (b) (d) M2, and (c) (e) M3.

3.2 Distribution of Fe and Ni in reduced Mo powders

Fig. 3a shows the XRD profiles of Mo powders prepared by hydrogen reduction of MoO_3 at 900 °C. The profound diffraction peaks at ~40.6°, ~58.7° and ~73.7° demonstrate that MoO_3 has been readily converted into metallic Mo (JCPDS 42-1120). No other phases containing Fe were detected for M2, probability due to the considerable solubility of iron in the Mo matrix,[27] while minor peaks of NiMo (JCPDS 48-1745) were identified for M3. The latter is not surprising because nickel is a low soluble element in Mo and Mo-Ni intermetallic phases can be easily formed upon heating.[7] The morphologies of reduced Mo powders are then illustrated in Fig. 3(b-d). It shows that pure Mo particles are rod-shaped (0.5-2 μm in length) and tend to agglomerate, while the doped Mo particles exhibit more spherical morphologies with an average particle size in the order of 1 μm. Uniform and dispersed Mo particles are desirable for the following PM processing.[28]

TEM analysis was conducted to identify the distribution of doping elements within reduced Mo powders. Fig. 4a is a HAADF micrograph of the ultrathin sections of Fe-doped Mo particle. As can be seen, Mo

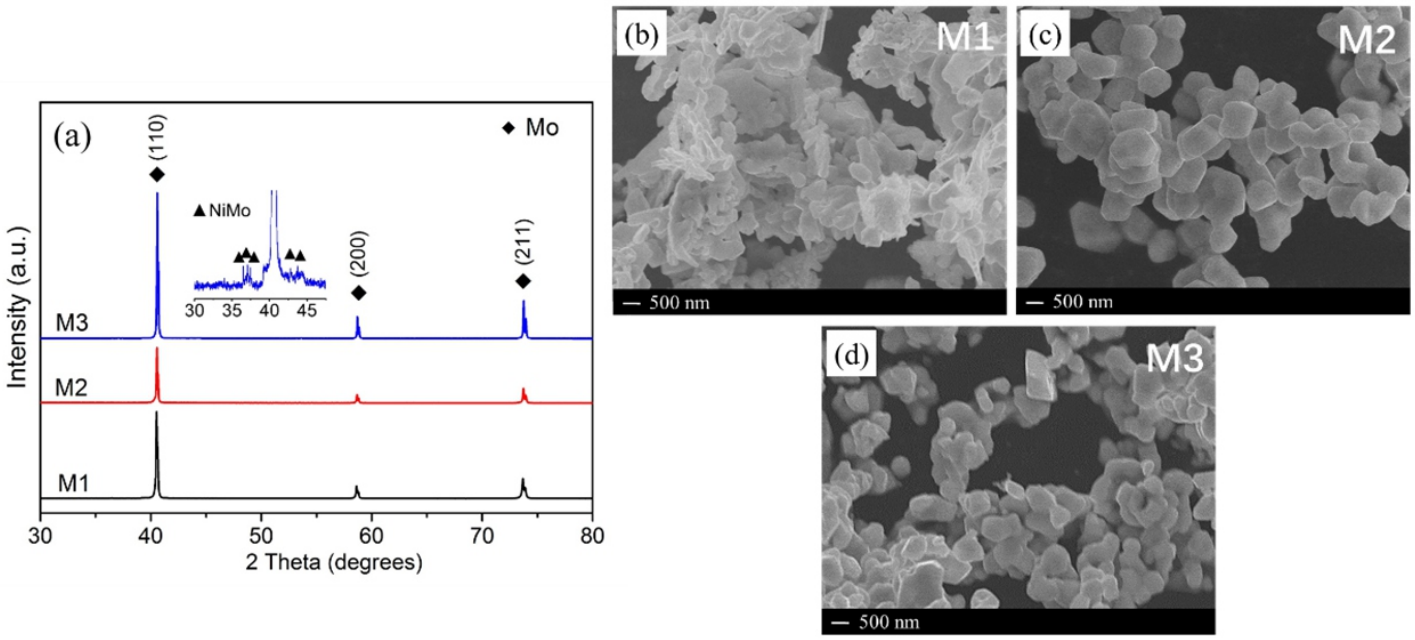

Fig. 3 XRD patterns (a) and morphologies (b-d) of reduced Mo powders.

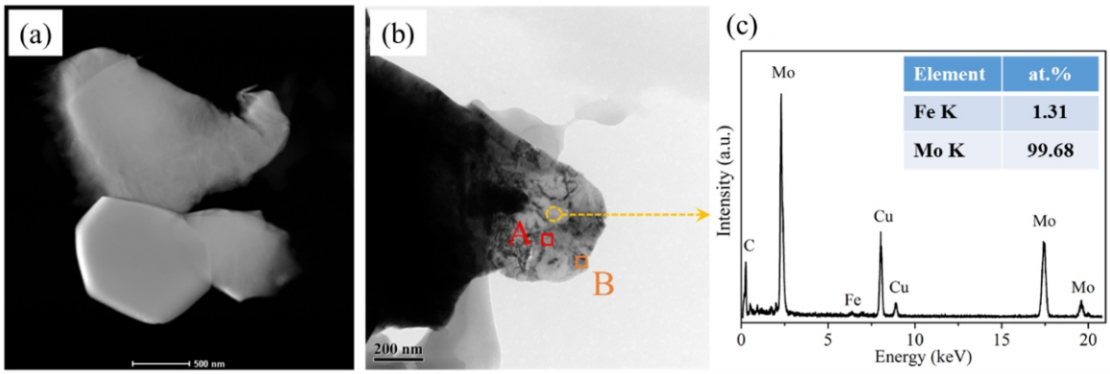

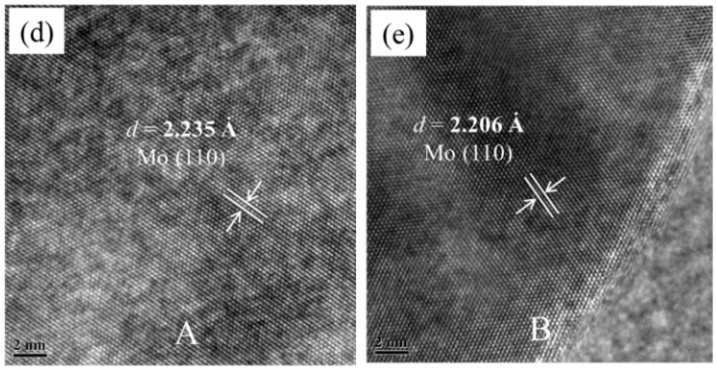

Fig. 4 STEM observation for 1.0 wt.% Fe doped Mo powders: (a) HAADF micrograph, (b) bright-field TEM image, (c) EDS spectrum and (d-e) HRTEM images.

exhibits a typical polyhedral morphology and no secondary phases are visible at the surfaces or interiors of these particles. Fig. 4b shows the bright-field TEM image taken from a typical region. The corresponding EDS spectrum in Fig. 4c confirms a presence of Fe and Mo within the powder (the signals of C and Cu are originated from the C-coated Cu grid). High-resolution TEM images collected at the marked location "A" and "B" in Fig. 4b are then presented in Fig. 4d-e, in which the lattice spacing are determined as 2.235 Å and 2.206 Å, respectively, aligned with the *d* value of (110) plane of the standard Mo specimen (2.225 Å). The lower d-spacing value also indicates a formation of Mo(Fe) solid solution at surface region. In order to provide direct evidence for impurity segregation, atom-resolved EDS analysis is highly demanded and this will be carried out in our future studies.

It is widely accepted the reduction of commercial MoO_3 takes place by chemical vapour transport and follows the reactions of $MoO_3 \rightarrow Mo_4O_{11} + MoO_2 \rightarrow MoO_2$ (at ~600 ºC) → Mo (at ~900 ºC).[29-31] W. Kuang *et al*. further reported that the reduction procedure for $Fe_2(MoO_4)_3$ occurred in sequential steps of $Fe_2(MoO_4)_3 \rightarrow \beta\text{-}FeMoO_4 + Mo_4O_{11}$ (at ~655 ºC) → $Fe_2Mo_3O_8 + MoO_2$ (at ~700 ºC) → Fe + Mo (at ~865 ºC) with rising temperatures.[32] In this case, metallic Fe was readily formed when Fe-doped MoO_3 powders were reduced at 900 ºC. The diffusion of Fe atoms along Mo particle surfaces (surface diffusion) and in the Mo grains (lattice diffusion) is likely to happen afterwards. The latter can be supported by the fact that the solubility of Fe in Mo in the equilibrium phase could reach ~1 wt.% at 900 ºC.[33] Moreover, K. Nohara *et al*. discovered the penetration depth of Fe in solid Mo was ~20 um after an intended diffusion annealing treatment at 1000 ºC for 533.3 h, while the majority of Fe atoms were still located at near surface regions.[34] Considering the reduction conditions employed in the present work, iron atoms reduced from $Fe_2(MoO_4)_3$ and Fe-MoO_{3-x} would be extremely difficult to penetrate in Mo grains at a long distance and turn to segregate at surfaces as solid solution.

Fig. 5 provides the TEM results for the Ni-doped Mo powders. As shown in the HAADF images (Fig. 5a), precipitates with bright contrast can clearly be observed on the particle surfaces. The corresponding EDS line scanning profiles (Fig. 5b) demonstrate that this cluster is rich with Mo and Ni, whereby the atomic ratio of Mo to Ni was found to be ~1 based on the EDS point findings in Fig. S3. The corresponding SAED patterns, taken from the bright-filed TEM image in Fig. 5c, further confirm that this secondary phase is NiMo (Fig. 5d) and the matrix is bcc-centred cubic Mo (Fig. 5e). Fig. 6f depicts a HRTEM image for the reduced Mo-Ni composite powders. It is seen that molybdenum is coated by a crystalline layer about 3-4 nm in thickness with a lattice spacing of 2.259 Å. Having compared with the lattice spacing values in Ni, Mo and various Mo-Ni compounds, the most likely phase of this coating layer is $Mo_{0.25}Ni_{0.75}$ (JCPDS 50-1094), which has been reported to be a metastable Ni-rich solid solution.[35,36] It is noteworthy that $Mo_{0.25}Ni_{0.75}$ is different with Ni_3Mo although they share the same chemical compositions. The latter is an intermetallic compound with orthorhombic structure and is known as a strengthening phase in nickel-based super alloy.[37]

As discussed earlier, the introduction of Ni into MoO_3 generated impurity atoms within lattice and produced $NiMoO_4$ at powder surfaces.

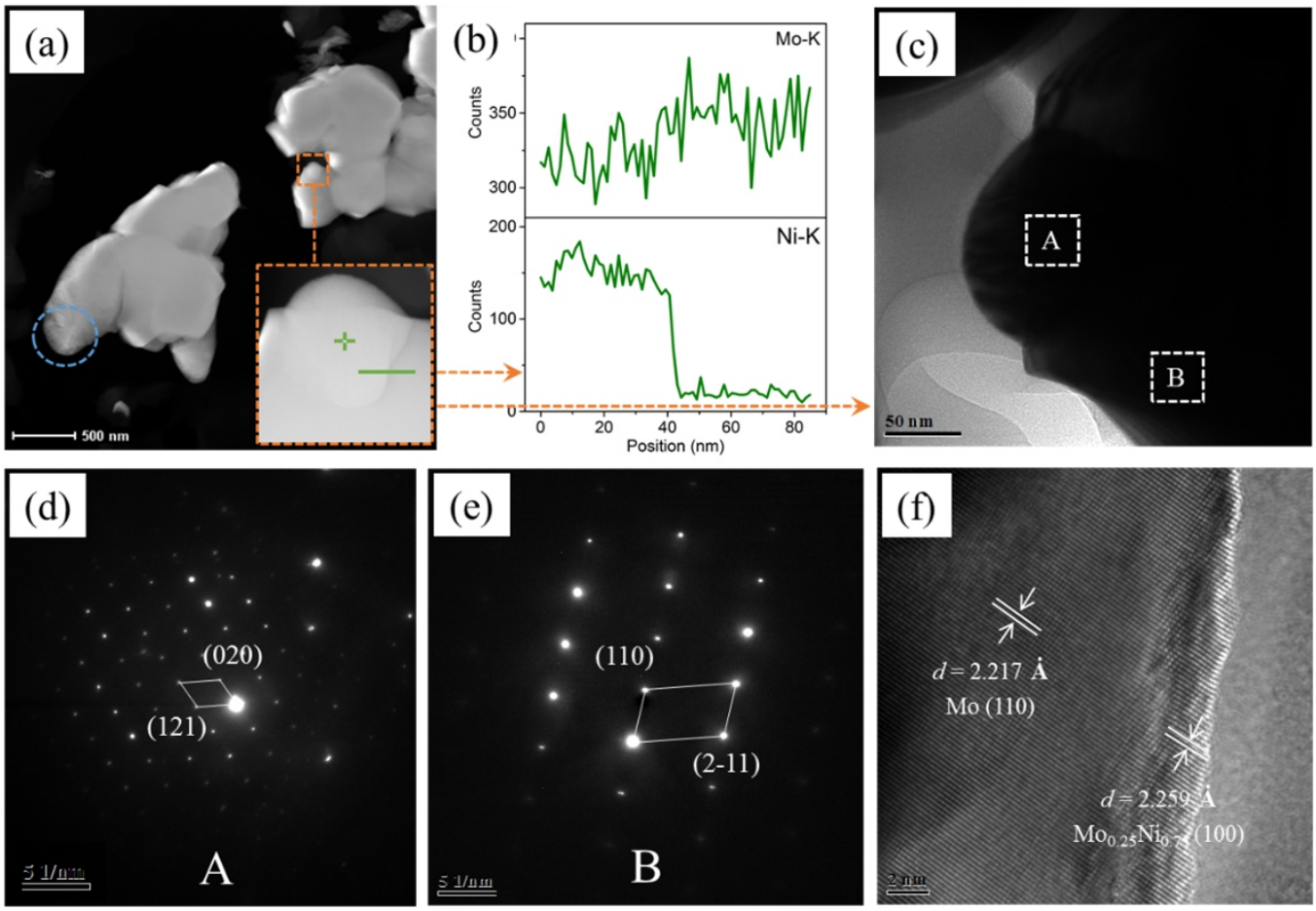

Fig. 5 STEM investigation for 1.0 wt.% Ni doped Mo powders: (a) HAADF micrographs, (b) EDS results along the scan line shown in (a), (c) bright-field TEM image, (d-e) SAED patterns and (f) HRTEM image collected at the circular marked in (a).

Among them, nickel molybdates was extensively investigated in recent years because this compound has proven to an effective catalyst for hydrodesulfurization reactions.[38,39] One representative work conducted by X. Tang *et al*. demonstrated that, when $NiMoO_4$ was reduced in hydrogen, two reduction processes would occur at 300-500 ºC and 500-700 ºC, corresponding to the conversion into metallic Ni and Mo, respectively.[40] H. Noukhlouf *et al*. provided more details regarding the first reducing reaction of $NiMoO_4 \rightarrow Ni + NiMo + MoO_2$[41] in which the NiMo compound has been reported to be thermally stable upto 1395 ºC.[42] It is therefore reasonable to infer that the NiMo particles observed in Fig. 5 should originate from the decomposition of $NiMoO_4$. Moreover, the Ni atoms reduced from $NiMoO_4$ and Ni-MoO_{3-x} may migrate through the Mo surfaces since fast surface diffusion of nickel on Mo and W are often observed.[7,43,44] Further interdiffusion between Mo and Ni would lead to the formation of intermetallics or solid solutions, but it is unclear why $Mo_{0.25}Ni_{0.75}$ was developed instead of other compounds.

3.3 Activated sintering mechanism in Fe/Ni doped Mo compacts

After powder preparation, pure and doped Mo compacts were fabricated and sintered at 1400 ºC for 1h in hydrogen atmosphere. The relative

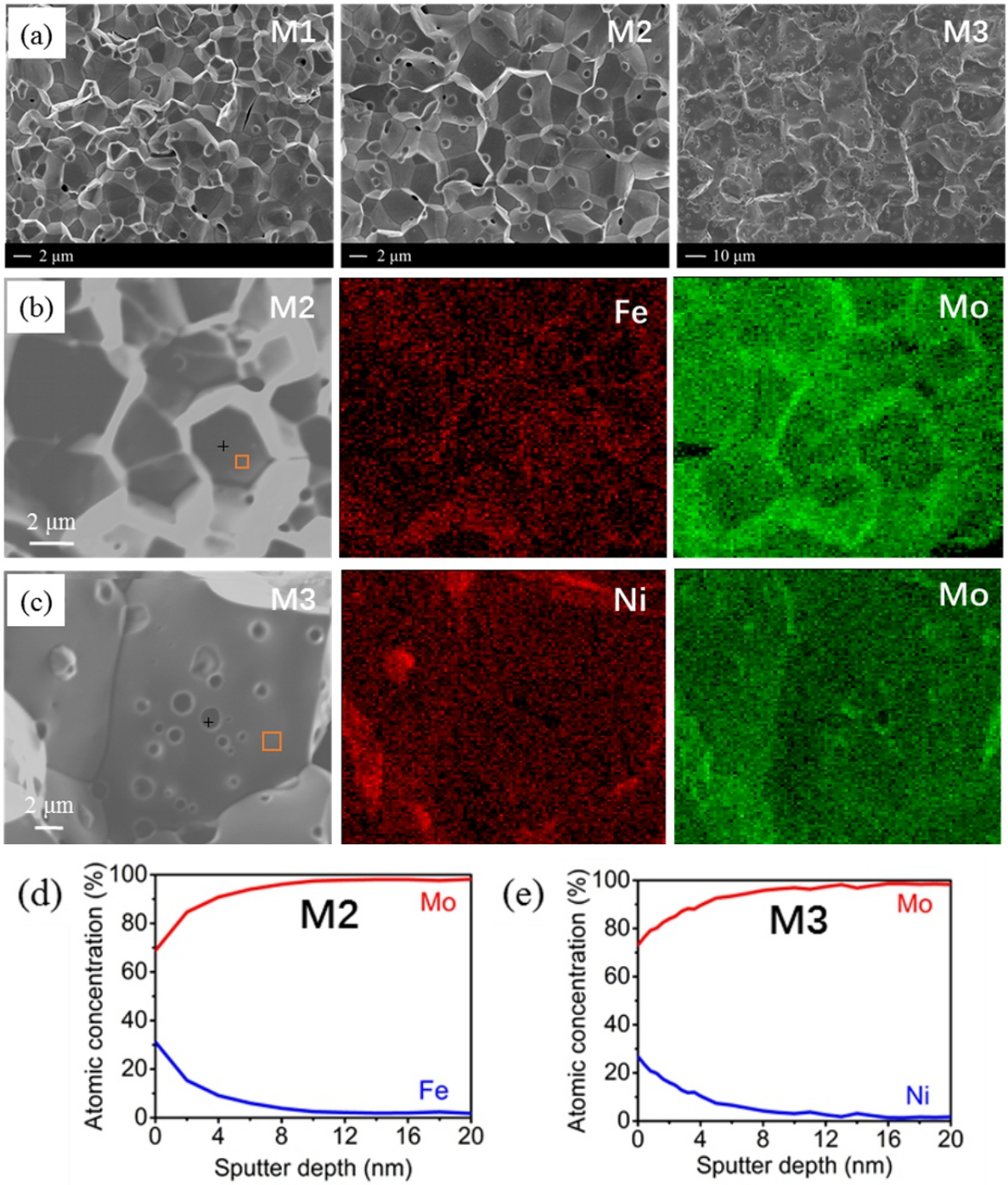

Fig. 6 SEM and AES analysis for the fractured surfaces of studied Mo compacts: (a) SEM images, (b-c) AES elemental maps and (d-e) depth profiles for M2 and M3, respectively.

densities of sintered specimen were firstly measured for evaluating the densification process. As shown in Table 1, the density value was increased from 83.5% for M1 to 90.9% for M2 and further to 97.2 % for M3, demonstrating that the transition metal additives greatly enhance the sinterability of Mo powders. The fractured morphologies of as-prepared Mo compacts are then illustrated in Fig. 6a. The intergranular fracture type of this sample suggests easy micro-cracks initiation and grows along the grain boundary (GB).[45] A large difference in grain size (2-6 μm in M1, 3-9 μm in M2 and 10-20 μm in M3, respectively) is also evident from the images. These structural observations prove that nickel is a more effective activator for the consolidation of molybdenum compared to iron. Furthermore, from the high-magnification micrograph of M3 (see Fig. S4), certain spherical particles can be clearly observed at grain boundaries. These secondary phases are rich with Ni and Mo, according to the corresponding EDS spectra in Fig. S4, and therefore can be assigned to the NiMo.

The fractured surfaces of doped Mo compacts were further examined by Auger electron microscope to identify the chemical distribution of Fe and Ni. From the Fe mapping maps in Fig. 6b, it is seen that iron is distributed homogeneously across the GB without any evidence of segregation even at the triple-grain junctions, indicating a solid-state sintering was occurred.[46] AES depth profiling was then conducted by sputtering with an argon ion beam. As observed in Fig. 6d, the atomic concentration of Fe decreases almost in a linear manner with increasing depth, representing Fe was mainly segregated at fractured GB. The penetration of iron atoms into Mo grains seems to be still difficult under a high temperature of 1400 ºC, which further confirms that the Mo(Fe) solid solution in reduced Mo powders are nanometer in thick. The GB segregation phenomenon can be detected in the Mo-Ni specimen as well (see Fig. 6c and e).

HRTEM observations were carried out to determine the microstructure of GB segregation layer. The TEM foils were cut with

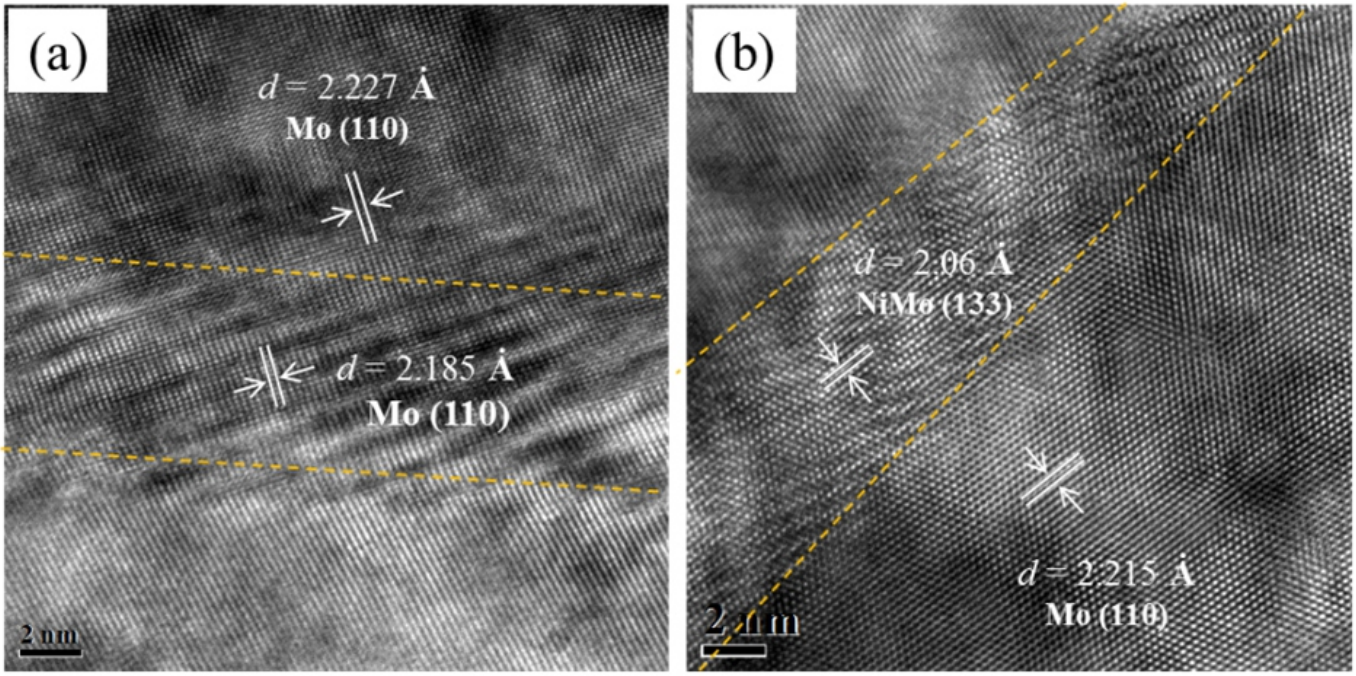

Fig. 7 HRTEM images of Fe-doped (a) and Ni-doped (b) Mo compact after sintering at 1400 ºC.

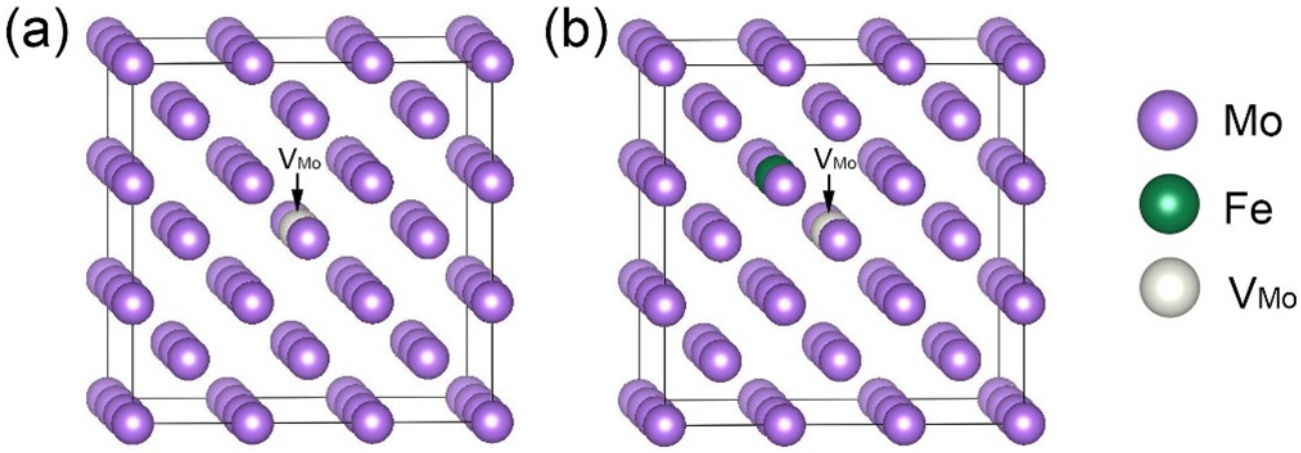

Fig. 8 Supercells of pure Mo (a) and Fe-doped Mo (b) used for calculations.

focused Ga ion beam. The low-magnification HAADF images in Fig. S5 indicates the segregation layers are continuous along the boundaries. From the HRTEM micrograph in Fig. 7a, obvious lattice distortions can be observed at the GB area of Mo-Fe compact, while the interfaces between GB and matrix seem to be coherent. The lattice spacing of the GB (2.185 Å) was found to be smaller than that of the adjacent grain (2.227 Å). This clearly demonstrates that the GB in Mo-1.0 wt.% Fe alloy are composed of Mo(Fe) solid solutions. Regarding Mo-Ni specimen, the HRTEM image in Fig. 7b depicts that the lattice fringes of matrix phases are distinct from the GB. The latter can be identified as NiMo after comparing its lattice spacing (2.06 Å) to a variety of Mo-Ni compounds. The thickness of the GB was estimated to be 6-9 nm and 3-7 nm for Fe/Ni doped Mo, respectively.

To explore the Fe-activated sintering mechanism in Mo, first-principles calculations have been carried out using the density-functional theory.[47-49] Fig. 8 shows a side view of an atom model diagram of pure Mo and Fe-doped Mo. The vacancy formation energy of Mo atom was calculated because one typical mechanism of atomic diffusion in the interior of solids is diffused through vacancies.[50] This formation energy, E_f, can be defined by equation $E_f = E_{vac} - (E_{bulk} - \mu_x)$, where E_{vac} and E_{bulk} are the total energies of pristine and vacancy containing supercells, respectively, μ_x is the total energy of a structure with one Mo atom.[51,52] The corresponding results in Table S1 demonstrate that it is easier to generate vacancies within Mo(Fe) solid solution compared to pure Mo. Therefore, Mo(Fe) could provide a diffusion path for Mo atoms along the boundaries and enhance the sintering activity considerably.

Different with Mo-Fe alloy system, the activated sintering mechanism in Mo-Ni alloy has been extensively investigated.[7,9,53] According to a representative work by K.S. Hwang et. Al,[7] the intergranular films of NiMo served as a short-circuit diffusion paths for Mo atoms and caused the solid-state activated sintering in nickel-doped molybdenum. It is noteworthy that the NiMo layer in K.S. Hwang et. al's work (~2 nm) is obviously thinner than that in ours, even they had employed 1.5 wt.% nickel into the system. This is something interesting to discuss because a thicker NiMo coating is beneficial for the mass transfer throughout sintering. The potential reason for the thicker NiMo layers in present study may relate to the pre-existence of $Mo_{0.25}Ni_{0.75}$ films at Mo powder surfaces, which can be easily transformed into NiMo upon heating to an elevated temperature. Furthermore, there is a higher possibility for the blended Mo-Ni composite powders (as used in K.S. Hwang et. al's work) to produce NiMo particles due to a compositional segregation, whereby less nickel can be utilized for the formation of NiMo films. Further efforts will be needed in order to make a complete conversion of the Ni additions into intergranular NiMo coatings.

4. Summary

In the present study, high densification Mo-1.0 wt.% Fe and Mo-1.0 wt.% Ni alloys were successfully fabricated by a powder metallurgy procedure. The distribution of Fe and Ni within MoO_3 and Mo powders were systematically investigated, before further correlating to the microstructural development of sintered molybdenum compacts. The main findings are summarized as follows:

(1) Both Fe and Ni had been incorporated into the lattice sites of MoO_3 after liquid-solid doping processing, while excess impurity atoms formed secondary phases of $Fe_2(MoO_4)_3$ and $NiMoO_4$ at surfaces of MoO_3. The existence of Fe/Ni-based species may affect the stacking behaviours of MoO_3 during annealing and result into refined microstructures.

(2) After hydrogen reduction, Mo(Fe) solid solution was formed at the surface region of reduced Mo powders, whereas $Mo_{0.25}Ni_{0.75}$ thin films and NiMo particles were detected at Mo surfaces.

(3) Solid-state activated sintering had occurred in Fe/Ni doped Mo compacts under a sintering temperature of 1400 ℃. The specimen density was increased from 83.5 % in pure Mo to 90.9 % in Mo-Fe alloy and further to 97.2 % in Mo-Ni alloy.

(4) The element of Fe was found to segregate at GB of Mo-Fe alloy as Mo(Fe) solid solution. First-principles calculation demonstrated that Mo(Fe) could promote the diffusion of Mo atoms by lowering the vacancy formation energy. Nanoscale NiMo segregation was identified at the fractured GB of Mo-Ni alloy. This NiMo layer was transformed from the $Mo_{0.25}Ni_{0.75}$ coating in Mo powders and served as a short-circuit diffusion paths for Mo atoms during sintering.

Author Contributions

H. Hu and Q. Yin contributed equally to this work.

Acknowledgments

This work was financially supported by National Key Research and Development of China (No. 2017YFB0305600), National Natural Science Foundation of China (No. 51471006, No. 51534009), National Natural Science Fund for Innovative Research Groups (No. 51621003), Beijing Municipal High Level Innovative Team Building Program (No. IDHT20170502). The authors would like to thank Dr. Xing Tang for helpful discussions in TEM analysis.

References

1. H. Materials, B. Yavas and G. Goller, *Int. J. Refract. Metals Hard Mater.*, 2019, **78**, 273–281.
2. S. Primig, H. Leitner and H. Clemens, *Int. J. Refract. Met. Hard Mater.*, 2010, **28**, 703–708.
3. M. A. Harimon, N. A. Hidayati, Y. Miyashita, Y. Otsuka, Y. Mutoh, S. Yamamoto and H. Aoyama, *Int. J. Refract. Met. Hard Mater.*, 2017, **66**, 52–56.
4. B. Yavas and G. Goller, *Int. J. Refract. Met. Hard Mater.*, 2016, **58**, 182–188.
5. R. Ohser-Wiedemann, C. Weck, U. Martin, A. Müller and H. J. Seifert, *Int. J. Refract. Met. Hard Mater.*, 2012, **32**, 1–6.
6. B. Basu, J. H. Lee and D. Y. Kim, *J. Am. Ceram. Soc.*, 2004, **87**, 1771–1774.
7. K. S. Hwang and H. S. Huang, *Acta Mater.*, 2003, **51**, 3915–3926.
8. K. S. Hwang and H. S. Huang, *Int. J. Refract. Met. Hard Mater.*, 2004, **22**, 185–191.
9. K. S. Hwang and H. S. Huang, *Mater. Chem. Phys.*, 2001, **67**, 92–100.
10. C. L. Chen and S. H. Ma, *J. Alloys Compd.*, 2017, **711**, 488–494.
11. Y. Han, J. Fan, T. Liu, H. Cheng and J. Tian, *Int. J. Refract. Met. Hard Mater.*, 2012, **34**, 18–26.
12. Q. Yin, C. Lai, S. Chen, J. Peng, H. Li, W. Zhou, P. Hu and J. Wang, *Int. J. Refract. Met. Hard Mater.*, 2019, **78**, 296–302.
13. X. L. Peng, *Mater. Sci. Eng. A*, 1999, **262**, 1–8.
14. Y. J. Chen, G. Xiao, T. S. Wang, F. Zhang, Y. Ma, P. Gao, C. L. Zhu, E. Zhang, Z. Xu and Q. Li, *Sensors Actuators B Chem.*, 2011, **155**, 270–277.
15. M. B. Rahmani, S. H. Keshmiri, J. Yu, A. Z. Sadek, L. Al-Mashat, A. Moafi, K. Latham, Y. X. Li, W. Wlodarski and K. Kalantar-zadeh, *Sensors Actuators B Chem.*, 2010, **145**, 13–19.
16. J. Shen, S. Guo, C. Chen, L. Sun, S. Wen, Y. Chen and S. Ruan, *Sensors Actuators B Chem.*, 2017, **252**, 757–763.
17. L. G. Pereira, L. E. B. Soledade, J. M. Ferreira, S. J. G. Lima, V. J. Fernandes, A. S. Araújo, C. A. Paskocimas, E. Longo, M. R. C. Santos, A. G. Souza and I. M. G. Santos, *J. Alloys Compd.*, 2008, **459**, 377–385.
18. Q. Y. Ouyang, L. Li, Q. S. Wang, Y. Zhang, T. S. Wang, F. N. Meng, Y. J. Chen and P. Gao, *Sensors Actuators, B Chem.*, 2012, **169**, 17–25.
19. X. Zhang, L. Wei and X. Guo, *Chem. Eng. J.*, 2018, **353**, 615–625.
20. R. Xu, N. Zhang, L. Sun, C. Chen, Y. Chen, C. Li and S. Ruan, *RSC Adv.*,

2016, **6**, 106364–106369.
21. M. Ahsan, T. Tesfamichael, M. Ionescu, J. Bell and N. Motta, *Sensors Actuators B Chem.*, 2012, **162**, 14–21.
22. Y. Huang, L. Cong, J. Yu, P. Eloy and P. Ruiz, *J. Mol. Catal. A Chem.*, 2009, **302**, 48–53.
23. Z. Zhang, X. Ma and J. Tang, *J. Mater. Chem. A*, 2018, **6**, 12361–12369.
24. C. Wang, G. Zhang and X. He, *Appl. Surf. Sci.*, 2010, **256**, 6047–6052.
25. J. Z. Ou, J. L. Campbell, D. Yao, W. Wlodarski and K. Kalantar-zadeh, *J. Phys. Chem. C*, 2011, **115**, 10757–10763.
26. K. Kalantar-zadeh, J. Tang, M. Wang, K. L. Wang, A. Shailos, K. Galatsis, R. Kojima, V. Strong, A. Lech, W. Wlodarski and R. B. Kaner, *Nanoscale*, 2010, **2**, 429–433.
27. Y. J. Baik and D. N. Yoon, *Acta Metall.*, 1986, **34**, 2039–2044.
28. X. Wang, J. Liu, F. E. I. Zhuang, H. U. Zhao and J. Li, *Metall. Mater. Trans. B*, 2010, **41**, 1067–1073.
29. J. Dang, G.-H. Zhang, K.-C. Chou, R. G. Reddy, Y. He and Y. Sun, *Int. J. Refract. Met. Hard Mater.*, 2013, **41**, 216–223.
30. R. K. Enneti, *Int. J. Refract. Met. Hard Mater.*, 2012, **33**, 122–123.
31. H. Xie, G. Zhang, D. Wang, Z. Lv, P. Zhao and S. Yuanjun, *Molybdenum Powder Metallurgy and Molybdenum Materials (Chinese Edition)*, Science Press, 2012.
32. W. Kuang, Y. Fan, K. Chen and Y. Chen, *J. Catal.*, 1999, **186**, 310–317.
33. *ASM Metals Handbook Alloy Phase Diagrams*, ASM International, 1992.
34. K. Nohara and K.Hirano, *J. Jpn. Inst. Met.*, 1973, **37**, 731–736.
35. Z. J. Zhang and B. X. Liu, *J. Appl. Phys.*, 1994, **76**, 3351–3356.
36. X. Y. H. and J. S. P. and Y. D. Fan, *Jpn. J. Appl. Phys.*, 1997, **36**, 1191.
37. L. Qi, Y. Jin, Y. Zhao, X. Yang, H. Zhao and P. Han, *J. Alloys Compd.*, 2015, **621**, 383–388.
38. B. Y. Kim, J. H. Ahn, J. W. Yoon, C. S. Lee, Y. C. Kang, F. Abdel-Hady, A. A. Wazzan and J. H. Lee, *ACS Appl. Mater. Interfaces*, 2016, **8**, 34603–34611.
39. H. Oudghiri-Hassani and F. Al Wadaani, *Molecules*.
40. X. Tang, L. Xiao, C. Yang, J. Lu and L. Zhuang, *Int. J. Hydrogen Energy*, 2014, **39**, 3055–3060.
41. H. Boukhlouf, R. Benrabaa, S. Barama and A. Barama, *Mater. Sci. Forum*, 2009, **609**, 145–148.
42. Y. Pan, Y. Du, J. Lv, T. Liang and F. Luo, *Thermochim. Acta*, 2018, **661**, 137–146.
43. G. H. Gessinger and H. F. Fischmeister, *J. Less Common Met.*, 1972, **27**, 129–141.
44. In-Hyung Moon, Ki-Youl Kim, Sung-Tag Oh and Myung-Jin Suk, *J. Alloys Compd.*, 1993, **201**, 129–137.
45. M. B. Shongwe, S. Diouf, M. O. Durowoju and P. A. Olubambi, *J. Alloys Compd.*, 2015, **649**, 824–832.
46. V. K. Gupta, D. H. Yoon, H. M. Meyer and J. Luo, *Acta Mater.*, 2007, **55**, 3131–3142.
47. C. Lai, J. Wang, F. Zhou, W. Liu, P. Hu, C. Wang, R. Wang and N. Miao, *Appl. Surf. Sci.*, 2018, **440**, 763–769.
48. C. Lai, J. Wang, F. Zhou, W. Liu and N. Miao, *J. Alloys Compd.*, 2017, **728**, 984–991.
49. C. Lai, J. Wang, F. Zhou, W. Liu, D. den Engelsen and N. Miao, *Appl. Surf. Sci.*, 2018, **427**, 874–882.
50. H. B. Huntington and F. Seitz, *Phys. Rev.*, 1942, **61**, 315–325.
51. J. Carrasco, N. Lopez and F. Illas, *Phys. Rev. Lett.*, 2004, **93**, 225502.
52. Y. Hua, J. Wang, J. Ma, S. Chen, C. Lai and D. den Englsen, *Int. J. Refract. Met. Hard Mater.*
53. J. T. Smith, *J. Appl. Phys.*, 1965, **36**, 595–598.